Check for updates

Enriched oxygen vacancies in SnO$_{2-x}$ with narrow bandgap for highly sensitive gas sensing†

Pei-Xuan Wu,[abc] Bo-Jing Ruan,[b] Ke-Feng Li,[abc] Wei-Hua Deng,*[a] Yong-Jun Chen*[b] and Gang Xu [ID][b]

High-performance SnO$_2$-based chemiresistive gas sensors were realized at room temperature by narrowing the bandgap to enhance photogenerated carrier separation. The resulting SnO$_{2-x}$ exhibited one of the highest responses and lowest LODs among room-temperature and light-activated NO$_2$ sensors. This work offers a promising strategy for next-generation, low-power gas sensing applications.

Monitoring the type and concentration of gaseous species has prominent significance in industrial production, environment protection, public security, health care, food safety and military aerospace.[1–5] Compared with other gas detection technologies, chemiresistive gas sensors convert the gas concentration into a resistance change as the readout signal, with advantages including low-cost, easy-operation, and on-line and real-time detection.[6–9] Semiconducting metal oxides (MOs), such as TiO$_2$, ZnO, SnO$_2$, and In$_2$O$_3$, are the most successful chemiresistive sensing materials due to their high sensitivity, fast response and good long-term stability.[10–14] However, the high working temperature increases the device manufacturing cost, which has limited the development of MOs in gas sensing applications.

To advance room-temperature MO-based gas sensors, photoactivation has emerged as a promising approach by leveraging photogenerated electron–hole pairs to enhance surface reactivity. For instance, ZnO/graphene oxide hybrids exhibit UV-enhanced NO$_2$ sensing due to improved charge separation,[15] while Au-decorated TiO$_2$ achieves visible-light activation *via* plasmonic effects.[16] Heterojunctions such as SnO$_2$–ZnO also promote carrier separation, boosting the response under solar light.[17]

However, these multi-component systems often encounter challenges related to complex fabrication, high cost, or stability issues. Additionally, the wide bandgaps of single MOs continue to limit the efficiency of photogenerated carrier separation, leading to unsatisfactory sensitivity at low concentrations. Therefore, improving electron–hole separation to increase the density of active sites under light is crucial not only for enabling room-temperature sensing but also for enhancing sensitivity. Reducing the bandgap can lower the energy barrier for photogenerated electron transition, thereby enhancing the separation efficiency of electrons and holes. In MOs, increasing oxygen vacancies presents a viable approach to reducing the bandgap.[18–22] This strategy not only improves the separation efficiency of electrons and holes but also offers the additional benefit of increasing the amount of oxygen adsorbed on the surface. To date, studies that leverage both advantages to significantly improve room-temperature sensing performance in MOs have not yet been reported.

Herein, we increase the number of oxygen vacancies in SnO$_2$ to reduce the bandgap by introducing Sn powder during the synthesis process. This approach lowers the bandgap, enhances the efficiency of charge separation under light, and increases the density of active sites, thereby significantly improving the gas sensing performance (Scheme 1). The resulting transparent SnO$_{2-x}$ devices exhibit a record-high response to 100 ppm NO$_2$ under visible-light, which is 500 times higher than that of SnO$_2$. This work not only enhances the photoactivated gas sensing performance of MOs but also offers practical potential for the development of room-temperature sensors suitable for air quality monitoring and industrial safety systems.
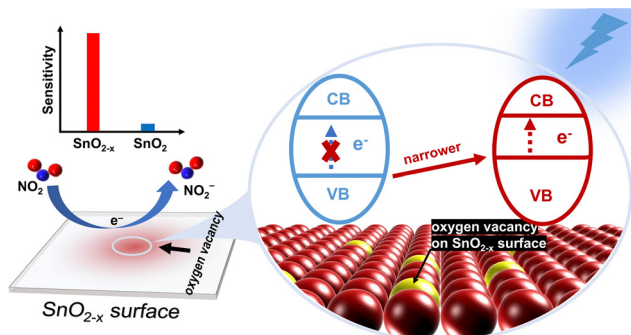
To prove that the structure of the obtained thin film is SnO$_{2-x}$, we collected a powder sample in the system of synthesizing SnO$_{2-x}$ thin film. The TEM images revealed that the powder sample is composed of small nanoparticles of 5–10 nm. The spacing between the adjacent lattice planes parallel to the growing direction is about 0.33 nm, which belongs to the (110) plane of rutile SnO$_2$ (Fig. 1c and d). Powder X-ray diffraction (PXRD) further confirmed that the obtained thin film is crystalline SnO$_2$. Both in-plane and out-of-plane diffraction patterns

^{a} College of Chemistry and Materials Science, Fujian Normal University, Fuzhou, Fujian 350007, P. R. China. E-mail: dengweihua@fjnu.edu.cn

^{b} State Key Laboratory of Structural Chemistry, and Fujian Provincial Key Laboratory of Materials and Techniques toward Hydrogen Energy, Fujian Institute of Research on the Structure of Matter, Chinese Academy of Sciences, Fuzhou, Fujian 350002, P. R. China. E-mail: chenyongjun@fjirsm.ac.cn

^{c} Fujian College, University of Chinese Academy of Sciences, Fuzhou, Fujian 350002, P. R. China

† Electronic supplementary information (ESI) available: Experimental details, Fig. S1–S13 and Table S1. See DOI: https://doi.org/10.1039/d5cc00960j

Scheme 1   Performance comparison between SnO$_2$ and SnO$_{2-x}$.

Fig. 2   SnO$_{2-x}$ thin film: (a) in-plane XRD pattern, (b) Tauc plot, (c) visible area transmittance, and (d) XPS spectra of the O 1s comparison between SnO$_2$ and SnO$_{2-x}$.

(Fig. 2a and Fig. S1, ESI†) matched the standard reference card (JCPDS no. 41-1445, rutile SnO$_2$), indicating high phase purity. The characteristic peaks at 26.6° and 33.8° correspond to the (110) and (101) crystal planes, respectively (Fig. 2a). The above results demonstrated that the SnO$_{2-x}$ thin film was successfully prepared.

It is worth noticing that the color of the SnO$_{2-x}$ powder sample (yellow) we synthesized is different from that of traditional SnO$_2$ (white). The reason was revealed by the characterization of UV/vis absorption and X-ray photoelectron spectroscopy (XPS). UV/vis absorption demonstrated that the optical bandgap of SnO$_{2-x}$ is 2.83 eV, which is narrower than that of the white SnO$_2$ (3.32 eV) (Fig. 2b, c and Fig. S2, S3, ESI†). X-ray photoelectron spectroscopy (XPS) evaluated the elemental composition and chemical states of the SnO$_{2-x}$ samples. The survey spectrum displayed peaks corresponding to C, O, and Sn, with no additional signals, indicating high elemental purity
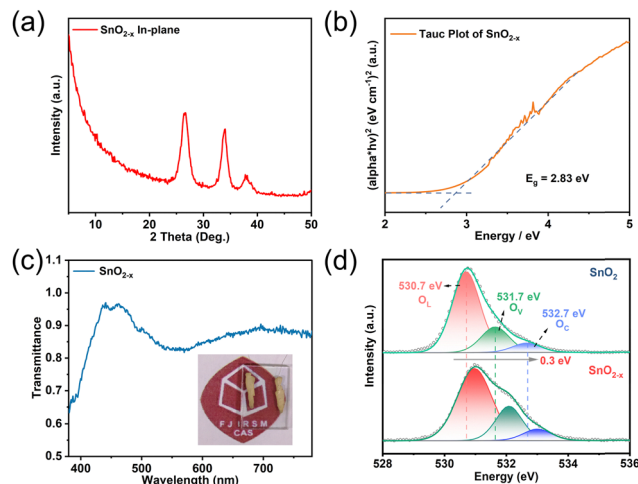
of the SnO$_{2-x}$ samples (Fig. S4, ESI† and Fig. 2d). The high-resolution Sn 3d spectrum revealed a chemical shift of approximately 8.4 eV between these two peaks, characteristic of Sn^{4+} in SnO$_2$. Deconvolution of the Sn 3d spectrum yielded four subcomponents: two for the 3d$_{5/2}$ and two for the 3d$_{3/2}$ states. The primary components appeared at 486.9 eV (3d$_{5/2}$) and 495.2 eV (3d$_{3/2}$), corresponding to Sn^{2+}. The lower-energy components at 487.2 eV (3d$_{5/2}$) and 495.6 eV (3d$_{3/2}$) are attributed to Sn^{4+} (Fig. S5, ESI†).[23,24] Compared with SnO$_2$, the increase in the O$_V$ peak intensity of SnO$_{2-x}$ and the uniform +0.3 eV shift in the XPS O 1s spectrum confirm oxygen vacancy enrichment, which correlates directly with enhanced surface adsorption and charge transfer capability (Fig. 2d and Fig. S6, ESI†).[23–26]

The narrow bandgap of the SnO$_{2-x}$ thin film with oxygen vacancies might serve as a desired platform for chemiresistive gas sensing. The SnO$_{2-x}$ thin film was tested within visible-light and at room temperature (RT) toward NO$_2$ in a self-made system (Fig. S7, ESI†). Detailed specifications of the setup are provided in the ESI.† SnO$_{2-x}$ nanostructures were grown on pre-cut glass substrates, with electrical contacts established using silver wires (diameter: 50 μm) and commercial silver paste (Fig. 3a). In the dark, the SnO$_{2-x}$ thin-film device exhibits a noticeable response of 2495 to 100 ppm NO$_2$ at room temperature, but with poor recovery. While recovery can be achieved by increasing the temperature to 80–150 °C, the corresponding response values are significantly reduced (Fig. 3b and Fig. S8, ESI†). In contrast, when exposed to visible light (λ = 450 nm, intensity = 18.67 mW cm^{-2}), the sensor shows a remarkable and reversible response upon cyclic exposure to NO$_2$ and dry air. Under continuous visible light illumination and at RT, the devices were exposed to NO$_2$ concentrations ranging from 20 ppb to 100 ppm, and exhibited a rapid, pronounced, and reversible response (Fig. 3c and Fig. S9, ESI†). The response of SnO$_{2-x}$ toward 100 ppm NO$_2$ is 20 553 under visible-light and at RT, which is the highest value for all reported NO$_2$ sensing materials (Fig. 3d and Table S1, ESI†).[17,27–36] Compared to its
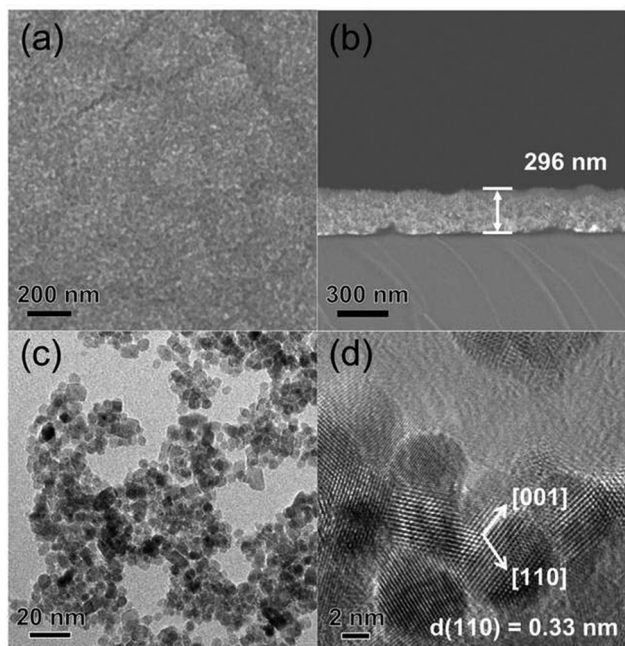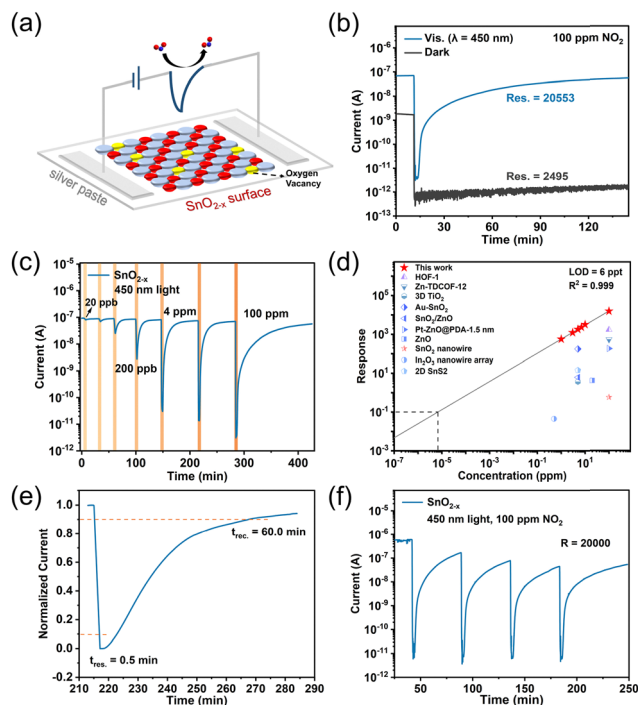

Fig. 1   (a) SEM surface view of SnO$_{2-x}$. (b) SEM cross sectional view of SnO$_{2-x}$. (c) TEM image of the basic morphology of the SnO$_{2-x}$ powder. (d) TEM image showing lattice stripes of SnO$_{2-x}$ powder.

Fig. 3 Sensing performances of the SnO_{2-x} thin film at RT: (a) SnO_{2-x} thin film device schematic, (b) response and recovery curves under dark and visible light conditions, (c) dynamic response–recovery curve to NO_2 with different concentrations under visible light, (d) responses comparison of reported NO_2 chemiresistive gas sensors, (e) normalized response–time curve to 10 ppm NO_2, and (f) multi-cycle response curve to 100 ppm NO_2.

performance under dark conditions, the response of the SnO_{2-x} film increased by 8.2 times under visible light irradiation (Fig. 3b). In addition, the response of SnO_{2-x} is 500 times higher than that of SnO_2 under the same conditions (Fig. S10, ESI†). These results demonstrated the effectiveness of bandgap narrowing induced by increased oxygen vacancies in enhancing the gas sensing performance of MOs.

To analyze the device time parameters, device response *versus* time was plotted after normalizing their current response values. The response time (90% signal raise) of the device when exposed to the NO_2 gas and the recovery time (signal retention to 10%) after the dry-air sweep were calculated (Fig. 3e and Fig. S11, ESI†). At 100 ppm NO_2, the response time was within 30 seconds, and it exhibits good repeatability (Fig. 3e and f). Meanwhile, by linear fitting the response–concentration relationship (Fig. 3d), a theoretical low limit of detection (LOD) of 6 ppt was extrapolated (when the response threshold is set as 10%), representing the lowest reported LOD among all NO_2 sensing materials to date (Fig. S7 and Table S1, ESI†).

The selectivity of the SnO_{2-x} thin film was further assessed by exposing the sensor to 14 common interfering gases, each at 100 ppm (Fig. S12a, ESI†). As shown in Fig. S12a (ESI†), the SnO_{2-x} sensor exhibited negligible responses to interference analytes with a high selectivity coefficient ($S = R_{NO_2}/R_{other\,gas}$) ranging from 3486 to 1 644 240. The measurements revealed outstanding selectivity of the SnO_{2-x} thin film device. The high sensor selectivity of SnO_{2-x} for NO_2 can be primarily attributed

to the electron enrichment associated with oxygen vacancies under light, as well as the strong oxidation of NO_2. The presence of oxygen vacancies alters the density of electron states near the surface of SnO_{2-x}, resulting in enhanced localization of electrons or holes under illumination. When NO_2 molecules adsorb onto the surface of SnO_{2-x} with oxygen vacancies, the charge transfer process occurs more readily. This phenomenon can be attributed to NO_2's strong oxidizing properties, which facilitate the extraction of electrons from electron-rich oxygen vacancies, thereby yielding a pronounced response to NO_2. The low response of SnO_{2-x} to SO_2 demonstrates this result (Fig. S12a, ESI†). In contrast, other gases typically exhibit weaker oxidizing characteristics and consequently elicit a less significant response. Additionally, the result of the humidity effect on sensing shows that interference based on the changing humidity is inevitable (Fig. S13 and S14, ESI†), which needs to be improved by some strategies to meet the actual test requirements.

We attribute the remarkable NO_2 sensing performance of SnO_{2-x} under visible light irradiation to originate fundamentally from the narrowing of the bandgap. This bandgap narrowing is achieved through oxygen vacancy increasing, which introduces donor states near the conduction band and distorts the local electronic structure, reducing the bandgap from 3.6 eV to 2.28 eV (Fig S12b, ESI†).[37,38] The reduced bandgap allows SnO_{2-x} to absorb 450 nm visible light efficiently, generating electron–hole pairs upon excitation. The photogenerated electrons facilitate charge exchange with surface oxygen species or directly transfer to NO_2 molecules, while holes promote oxygen desorption, resulting in improved response and accelerated recovery.[39,40] The presence of oxygen vacancies further enhances these light-driven processes. Furthermore, the superior response under 450 nm illumination is attributed to the synergistic effect of bandgap narrowing and oxygen-vacancy-induced defect states, which facilitate sub-bandgap absorption and photogenerated charge carrier separation. In contrast, broad-spectrum irradiation introduces excess high-energy photons, which elevate non-radiative relaxation and recombination, thereby reducing the effective carrier density for gas sensing.[25,26]

Based on the above discussion, the sensing mechanism can be described as follows. Firstly, oxygen vacancies act as carrier trapping centers, extending the lifetime of photogenerated carriers and reducing recombination loss. Secondly, oxygen vacancies function as active adsorption sites, increasing the density of chemisorbed oxygen species (O_2^-, O^-), which extract electrons from the conduction band and form a surface depletion layer. Upon NO_2 exposure, these adsorbed oxygen species and NO_2 undergo charge exchange, further depleting electrons and modulating the resistance (Fig S12c, ESI†).

In summary, enriched oxygen vacancies in SnO_{2-x} thin film achieve a reduction in bandgap from 3.32 eV to 2.83 eV, enabling visible-light activation for RT NO_2 sensing. Under 450 nm irradiation, the sensor exhibited a high response ($\sim$20 000) and a theoretical LOD down to 6 ppt, with rapid recovery. The performance enhancement is attributed to the synergistic effect of oxygen vacancies enhancing surface

adsorption and bandgap narrowing promoting photogenerated charge separation. This work demonstrates a cost-effective strategy for visible-light-driven gas sensors, offering insights into band structure tuning for future low-power environmental monitoring applications.

Data availability

The data supporting this article have been included as part of the ESI.†

Conflicts of interest

There are no conflicts to declare.

Notes and references

1 E. González, J. Casanova-Chafer, A. Romero, X. Vilanova, J. Mitrovics and E. Llobet, *Sensors*, 2020, **20**, 6225.
2 A. Khorramifar, M. Rasekh, H. Karami, J. A. Covington, S. M. Derakhshani, J. Ramos and M. Gancarz, *Molecules*, 2022, **27**, 3508.
3 X. Jia, P. Qiao, X. Wang, M. Yan, Y. Chen, B.-L. An, P. Hu, B. Lu, J. Xu, Z. Xue and J. Xu, *Nano-Micro Lett.*, 2024, **16**, 136.
4 Y. Wang, X. Yan, S. Wang, S. Gao, K. Yang, R. Zhang, M. Zhang, M. Wang, L. Ren and J. Yu, *Environ. Res.*, 2023, **227**, 115677.
5 I. G. Van Der Sar, C. C. Moor, J. C. Oppenheimer, M. L. Luijendijk, P. L. A. Van Daele, A. H. Maitland-van Der Zee, P. Brinkman and M. S. Wijsenbeek, *Chest*, 2022, **161**, 738–747.
6 S. M. Kanan, O. M. El-Kadri, I. A. Abu-Yousef and M. C. Kanan, *Sensors*, 2009, **9**, 8158–8196.
7 M. E. Franke, T. J. Koplin and U. Simon, *Small*, 2006, **2**, 36–50.
8 T. Wagner, S. Haffer, C. Weinberger, D. Klaus and M. Tiemann, *Chem. Soc. Rev.*, 2013, **42**, 4036–4053.
9 D.-B. Moon, A. Bag, H. H. Chouhdry, S. J. Hong and N.-E. Lee, *ACS Sens.*, 2024, **9**, 6071–6081.
10 P. Vafaei, M. Kodu, H. Alles, V. Kiisk, O. Casals, J. D. Prades and R. Jaaniso, *Sensors*, 2025, **25**, 382.
11 J. Xu, X. Fan, K. Xu, K. Wu, H. Liao and C. Zhang, *Nano-Micro Lett.*, 2025, **17**, 115.
12 Y. Qu and J. Zhang, *ACS Appl. Electron. Mater.*, 2025, **7**, 865–873.
13 R. Thekke Parayil, S. Paine, K. Mukherjee, D. Tyagi, M. Mohapatra and S. K. Gupta, *Phys. Chem. Chem. Phys.*, 2025, **27**, 2817–2827.
14 P. Cao, X. Xu, F. Jia, Y. Zeng, W. Liu, C. Wang, S. Han, M. Fang, X. Liu, D. Zhu and S. T. Navale, *Appl. Surf. Sci.*, 2025, **688** 162424.
15 Y. Zhai, D. Liu, Y. Jiang, X. Chen, L. Shao, J. Li, K. Sheng, X. Zhang and H. Song, *Sens. Actuators, B*, 2019, **286**, 468–475.
16 F. Khatun, A. Abd Aziz, L. C. Sim and M. U. Monir, *J. Environ. Chem. Eng.*, 2019, **7**, 103233.
17 N. Liu, H. Yu, Y. Yang and X.-T. Dong, *IEEE Sens. J.*, 2020, **20**, 2852–2859.
18 S. R. Ch, L. Zhang, T. Kang, Y. Lin, Y. Qiu and S. R. A., *Ceram. Int.*, 2018, **44**, 4586–4591.
19 J. Wang, Z. Wang, B. Huang, Y. Ma, Y. Liu, X. Qin, X. Zhang and Y. Dai, *ACS Appl. Mater. Interfaces*, 2012, **4**, 4024–4030.
20 C.-M. Fan, Y. Peng, Q. Zhu, L. Lin, R.-X. Wang and A.-W. Xu, *J. Phys. Chem. C*, 2013, **117**, 24157–24166.
21 D. H. Jara, K. G. Stamplecoskie and P. V. Kamat, *J. Phys. Chem. Lett.*, 2016, **7**, 1452–1459.
22 A. Ayeshamariam, S. Ramalingam, M. Bououdina and M. Jayachandran, *Spectrochim. Acta, Part A*, 2014, **118**, 1135–1143.
23 C.-M. Fan, Y. Peng, Q. Zhu, L. Lin, R.-X. Wang and A.-W. Xu, *J. Phys. Chem. C*, 2013, **117**, 24157–24166.
24 C. Wang, G. Du, K. Ståhl, H. Huang, Y. Zhong and J. Z. Jiang, *J. Phys. Chem. C*, 2012, **116**, 4000–4011.
25 H. Zhou, R. Deng, Y.-F. Li, B. Yao, Z.-H. Ding, Q.-X. Wang, Y. Han, T. Wu and L. Liu, *J. Phys. Chem. C*, 2014, **118**, 6365–6371.
26 J. V. N. De Palma, A. C. Catto, M. C. De Oliveira, R. A. P. Ribeiro, M. D. Teodoro and L. F. Da Silva, *Sens. Actuators*, 2022, **4**, 100081.
27 K. Lim, Y.-M. Jo, J.-W. Yoon, J.-S. Kim, D.-J. Lee, Y. K. Moon, J. W. Yoon, J.-H. Kim, H. J. Choi and J.-H. Lee, *Small*, 2021, **17**, 2100438.
28 W.-H. Deng, L. He, E.-X. Chen, G.-E. Wang, X.-L. Ye, Z.-H. Fu, Q. Lin and G. Xu, *J. Mater. Chem. A*, 2022, **10**, 12977–12983.
29 Y.-J. Chen, M. Liu, J. Chen, X. Huang, Q.-H. Li, X.-L. Ye, G.-E. Wang and G. Xu, *Chem. Sci.*, 2023, **14**, 4824–4831.
30 Q. Liu, Y. Wen, J.-Z. Xiao, S.-Z. Luo, G.-E. Wang, P.-Y. Tang, X.-L. Ye and G. Xu, *Chin. J. Struct. Chem.*, 2023, **42**, 100069.
31 L. Meng, Q. Xu, Z. Sun, G. Li, S. Bai, Z. Wang and Y. Qin, *Mater. Lett.*, 2018, **212**, 296–298.
32 X.-X. Wang, H.-Y. Li and X. Guo, *J. Mater. Chem. A*, 2020, **8**, 14482–14490.
33 T. Hoon Eom, S. Hwan Cho, J. Min Suh, T. Kim, T. Hyung Lee, S. Eon Jun, J. Wook Yang, J. Lee, S.-H. Hong and H. Won Jang, *J. Mater. Chem. A*, 2021, **9**, 11168–11178.
34 Y.-J. Chen, Y.-Y. Wen, W.-H. Li, Z.-H. Fu, G.-E. Wang and G. Xu, *Nano Lett.*, 2023, **23**, 3614–3622.
35 S. Park, S. An, Y. Mun and C. Lee, *ACS Appl. Mater. Interfaces*, 2013, **5**, 4285–4292.
36 M. Al-Hashem, S. Akbar and P. Morris, *Sens. Actuators, B*, 2019, **301**, 126845.
37 C. Zhang, G. Liu, X. Geng, K. Wu and M. Debliquy, *Sens. Actuators, A*, 2020, **309**, 112026.
38 C. Zhang, X. Geng, J. Li, Y. Luo and P. Lu, *Sens. Actuators, B*, 2017, **248**, 886–893.
39 X. Geng, D. Lahem, C. Zhang, C.-J. Li, M.-G. Olivier and M. Debliquy, *Ceram. Int.*, 2019, **45**, 4253–4261.
40 A. Chizhov, M. Rumyantseva and A. Gaskov, *Nanomaterials*, 2021, **11**, 892.